An Unsteady Long Bearing Squeeze Film Damper Model
Part I: Circular Centered Orbits

P. A. Schallhorn, D. A. Elrod, D. G. Goggin, A. K. Majumdar

Sverdrup Technology, Inc.
Huntsville, Alabama 35806

ABSTRACT

This paper, the first of a two-part series, presents results of an unsteady rotordynamic analysis of a long-bearing squeeze film damper executing circular centered orbits using a fluid circuit approach. A series of nodes and branches represent the geometry of the flow circuit. The mass and momentum conservation equations are solved to predict the pressure distribution in the squeeze film. The motion of the bearing is simulated by the variation of geometry within the flow path. The modeling methodology is benchmarked against published experimental long-bearing squeeze film damper test results. The model provides good agreement with the experimental damping coefficient.

Nomenclature

C   Squeeze film damper radial clearance (difference in radii)

C_p $= \mu \omega R^2 / C^2$ Pressure conversion factor

C_{tt} $= -f_t/\varepsilon$ Dimensionless direct damping coefficient

d   Damper journal diameter

D_π $= f_r/\varepsilon$ Dimensionless direct inertia coefficient

e   Dynamic eccentricity (orbit radius)

L   Damper journal length

$\dot{m}$ Mass flow rate

p   Local pressure within the squeeze film region

r   Radial coordinate

R   Damper journal radius

Re $= \rho\omega C^2/\mu$ Reynolds number

z   Axial coordinate

ε $= e/C$ Eccentricity ratio (dimensionless orbit radius)

θ Circumferential coordinate

μ Fluid absolute viscosity

ρ Fluid density

τ_f Shear stress

ω Frequency of damper journal (whirl frequency)

Introduction

Squeeze film dampers (SFD) have been used to provide damping in high speed

rotating machinery with rolling element bearings for years. Extensive research has

been performed both experimentally and analytically to examine the effects of

geometry, cavitation, Reynolds number, etc. on squeeze film damper pressures and

forces. The experimental work of Jung et al.[1,2] examined the pressure distributions

and force coefficients for a squeeze film damper executing circular centered orbits for both open ended (short bearing) and partially sealed (long bearing) configurations. Analytical, circular-centered orbit, SFD models have been published for a variety of Reynolds numbers for both long bearing (axial flow neglected) and short bearing (circumferential flow neglected) assumptions. Analytical work by San Andres[3-6] and Tichy[7-9] addressed the effects of fluid inertia on both short and long bearing squeeze film dampers, and the effect of turbulence on short bearing squeeze film dampers. Recently, Schallhorn, *et al.*[12], described a fluid circuit approach for modeling long bearing squeeze film damper rotordynamics. In this paper, a steady state modeling technique, utilizing a fluid network code, was described and the technique was benchmarked against published experimental data. That modeling technique has been extended to an unsteady model of the damper by Schallhorn[13, 14].

This paper presents the results of the unsteady modeling for a long bearing squeeze film damper executing circular orbits. Comparisons of the unsteady analytical predictions to the experimental work of Jung *et al.*[2] are presented.

Fluid Flow Code

A general purpose, one-dimensional, network flow analysis computer code was chosen as the platform for SFD modeling[10]. The code uses a series of nodes and branches to define a flow network. Nodes are positions within the network where fluid properties (pressure, density, etc.) are either known or calculated. Branches are the portions of the flow network where flow conditions (geometry, flow rate, etc.) are

3

known or calculated. The code uses a finite volume approach with a staggered grid. This approach is commonly used in computational fluid dynamics schemes (Patankar[15], Patankar and Karki[16]). The staggered grid approach uses overlapping control volumes where the conservation of mass and the conservation of momentum are calculated in separate control volumes. For a conventional grid where only one control volume is used for both scalar and vector quantities, interpolation is required in formulating the conservation of the scalar quantities at the edges of the control volume and numerical errors result. For a staggered grid, however, mass flow rates are available at the surface of the continuity control volume and do not have to be interpolated.

Governing Equations

The primary governing equations used in this analysis are the continuity momentum equations. Additionally, two auxiliary equations are necessary for closure of the unknown variables. These auxiliary equations consist of the energy equation and the equation of state. Equations 1 and 2 are the unsteady governing equations used in the analysis. Equation 1 is the unsteady continuity equation for the flow into a node, where $\sum \dot{m}_{in}$ is the summation of flow into a node through the branches connecting to it, $\sum \dot{m}_{out}$ is the summation of flow out of a node through the branches connecting to it and $\dot{m}_{source}$ is a mass source term (which accounts for any other mass flow into or out of the node). Equation 2 represents the one-dimensional conservation of momentum for a branch in the flow network, where Δp is the pressure difference

across the branch, $A_{cross\ Section}$ is the cross-sectional area, L is the flow path length in a segment of the damper, ρ is the density of the fluid, u is the fluid velocity, v is the normal velocity of the inner segment of the damper, A_{normal} is a segmented area of the inner race corresponding to its normal velocity, τ_f is the shear stress and A_{Shear} is the shear area.

$$\sum \dot{m}_{in} + \dot{m}_{source} - \sum \dot{m}_{out} = \left(\frac{m_t - m_{t-\Delta t}}{\Delta t} \right)_{C.V.} \qquad (1)$$

$$\frac{\Delta(\dot{m}L)}{\Delta t} + \rho v \left(u_{inner\ segment} - u_{fluid} \right) A_{normal} = -A_{Cross\ Section} \Delta p - \tau_f A_{shear} \qquad (2)$$

Equations 1 and 2 are solved in a simultaneous solution iterative scheme (Newton-Raphson scheme) in order to obtain the branch flow rates and node pressures.

In order to obtain the mass resident in a node at a given time, an additional equation is necessary. The equation chosen to satisfy the unknown resident mass was the generalized equation of state; however, temperature is necessary for the state equation. In order to satisfy the requirement for temperature in the state equation, the energy conservation equation is used. Equation 3 is the energy equation used in the code, where h is the enthalpy of the fluid (from which temperature can be obtained) and $\dot{Q}_{Source}$ is any additional heat source added to the fluid. Note that the term, $pA_{normal}v$, represents the work done on the fluid by the inner segment of the damper

(i.e. the work done on a fluid by a moving boundary). Equation 4 is the generalized equation of state used in the code, where R is the gas constant of the fluid, T is the temperature of the fluid and Z is the compressibility of the fluid.

$$\sum \dot{m}_{in} h_{in} + \dot{Q}_{Source} + pA_{normal}v - \sum \dot{m}_{out}h_{out}$$
$$= \frac{\left[m\left(h - \frac{p}{\rho}\right)\right]_t - \left[m\left(h - \frac{p}{\rho}\right)\right]_{t-\Delta t}}{\Delta t} \qquad (3)$$

$$m = \frac{pV}{RTZ} \qquad (4)$$

Unsteady Long Bearing Squeeze Film Damper Modeling

The model used in the analysis is shown schematically in Figure 1. In the analysis, the bearing remains wrapped; however, curvature is neglected since the clearance to radius ratio is small (~1/40). This model varies from prior steady state modeling performed by the authors[12]. The motion of the inner race of the damper is simulated by the variation of the geometry of the flow path, as is illustrated in Figure 2. This geometry variation generates a pressure variation around the circumference of the damper. For rotordynamics applications, the pressure distribution of the fluid circuit model is integrated to obtain the radial and tangential forces of Equations 5 and 6.

$$F_r = \int_0^{2\pi} pA_{normal}\cos\theta d\theta \qquad (5)$$

$$F_t = \int_0^{2\pi} pA_{normal}\sin\theta d\theta \qquad (6)$$

In a dimensionless form, the radial and tangential forces are calculated using Equations 7 and 8, where Cp is the pressure coefficient defined in the nomenclature.

$$f_r = \int_0^{2\pi} \frac{p}{C_p} \cos\theta \, d\theta \qquad (7)$$

$$f_t = \int_0^{2\pi} \frac{p}{C_p} \sin\theta \, d\theta \qquad (8)$$

In rotordynamic models, these force components are represented by rotordynamic coefficients. These coefficients are analogous to the mass, damping and stiffness terms for a spring-mass-damper system. For an uncavitated squeeze film damper, the only two coefficients which occur are a radial inertia (or added mass) term, D_{rr}, and a circumferential damping term, C_{tt}. In order to compare with published experimental results[2], the damping and inertia coefficients are normalized by the eccentricity ratio and pressure coefficient, equations 9 and 10. Equation 9 is the non-dimensional circumferential damping coefficient and Equation 10 is the non-dimensional radial inertia coefficient.

$$C_{tt} = -f_t/\varepsilon \qquad (9)$$

$$D_{rr} = f_r/\varepsilon \qquad (10)$$

Squeeze Film Damper Experimental Benchmark

The experimental results of Jung, *et al.*[2] were used to validate the modeling methodology. The experimental work simulated a long bearing SFD by using an O-ring seal on one side of the bearing, and a serrated piston ring on the other side of the bearing to limit axial flow. A Reynolds number of 49.0 and an eccentricity ratio of 0.82 were chosen for comparison as the data indicates that cavitation was not present.

Results

Figure 3 shows the pressure profile of the benchmark squeeze film damper model compared with Jung's[2] experimental results. The pressure has been non-dimensionalized using equation 16 for comparison with Jung's published data.

$$\frac{p}{p_{reference}} = \frac{p}{Cp\,Re} = \frac{p}{\rho R^2 \omega^2} \tag{11}$$

The predicted pressure profile follows a similar trend as the experimental data. The predicted pressure profile deviates from the experimental results in the low pressure region; however, the model is able to predict the phase shift observed in the experimental benchmark, unlike an earlier published steady state model[12]. The rotordynamic coefficients for the benchmark model are presented in Table 1, along with Jung's experimentally derived coefficients. As Table 1 indicates, the damping coefficient predicted using the unsteady model lies just inside of the uncertainty band of Jung's experimental data. It should be noted that the uncertainty analysis derived

in reference 13 is very conservative (in favor of Jung, *et al.*); therefore, the unsteady model prediction is most likely to be well within the actual uncertainty band if all error sources were accounted for. The unsteady model dramatically over predicts the inertia coefficient compared to Jung's experimental results (unlike the steady state model which substantially under predicts the inertia coefficient). Figure 4 demonstrates the periodic nature of the model. The pressure profile shown in Figure 4 follows the variation in the clearance during the orbit (Figure 2); therefore verifying that for circular centered orbits, any snapshot in time should produce the same rotordynamic coefficients.

Parametric Studies

A set of parametric studies was performed on the unsteady model to observe the behavior of the model under various conditions for circular centered orbits. The first parametric study examined the variation of the Reynolds number for a fixed orbit size. The second parametric study examined the variation of orbit size for various Reynolds numbers.

Parametric Study on Reynolds Number for Fixed Orbit Size

In order to compare the unsteady model with the results of the benchmark experimental work[2], a parametric study on the prediction of rotordynamic coefficients over a range of Reynolds numbers was performed. This study was carried out for the following Reynolds numbers: 15, 25, 35, 49 and 75. Figure 5 shows the

dimensionless pressure profiles for Reynolds numbers 15, 25, 35, and 75, respectively.

Figures 6 and 7 show the coefficients predicted by this parametric study compared to Jung's experimental data and his prediction. In Figure 6, the unsteady model over-predicts the damping coefficient by ~ 10-15%, when compared with the test data (considered excellent agreement in rotordynamics). It is noted, however, that the experimental data has significant scatter and the precision uncertainty has not been included in the uncertainty estimate. The model prediction of the damping coefficient is an improvement over Jung's analytical prediction. As Figure 7 shows, the unsteady model over-predicts the inertia coefficient compared with the experimental data. The reason for this over prediction is the difference between the predicted and experimental pressure at the position of lowest pressure (see Figure 3 for $0 < \theta < 1$).

Parametric Study on Orbit Size for Various Reynolds Numbers

A parametric study was performed to examine the effect of orbit size (orbit radius) on the prediction of rotordynamic coefficients. Three orbit eccentricity ratios (ε) were chosen for the study: ε = 0.25, 0.50, and 0.82, respectively. Recall that ε = 0.82 is the eccentricity ratio of the benchmark case. Figures 8 and 9 are the dimensionless pressure profiles for eccentricities of ε = 0.25 and ε = 0.50 at three Reynolds numbers: 15, 49, and 75, respectively. Figure 10 is an overlay of the pressure profile for the three orbit sizes at a Reynolds number of 49. As orbit size decreases, the

circumferential pressure variation reduces and becomes less skewed (the curvature on the low pressure end resembles that of the high pressure end). As a result, the damping coefficient and force decrease with decreasing orbit size.

The predicted dimensionless rotordynamic coefficients are shown in Figures 11 and 12. Figure 11 illustrates that the dimensionless damping coefficient increases with increasing orbit size and Reynolds number. In Figure 12, the dimensionless inertia coefficient decreases with increasing orbit, the opposite of damping. However, in the definitions of these coefficients, the eccentricity ratio appears in the denominator (see Equations 9 and 10). It is this division by ε which causes the reversal in order between Figures 11 and 12; therefore two additional figures (Figures 13 and 14) are provided to illustrate the non-dimensional tangential and radial forces (which correspond to the damping and inertia forces, respectively, see Equations 7 and 8).

Figure 13 further illustrates that the tangential (i.e. damping) force increases with increasing orbit size. This result is expected based upon rotordynamic theory[6]. In Figure 14, however, the effect of orbit size on the radial (i.e. inertia) force is inconclusive, since the orbit size does not appear to correlate with the radial force. This lack of correlation is most likely due to the over-prediction of the low pressure region, as was seen in the comparison between the unsteady GFSSP prediction and experimental data for the benchmark case (Re = 49, ε_d = 0.82).

Conclusions

An unsteady long bearing squeeze film damper (SFD) rotordynamic analysis has been developed and successfully implemented. The approach uses a general one dimensional fluid flow code in which shear stress is calculated using friction factors. The motion of the rotor is simulated by variation of the geometry of the flow circuit and accounting for the affect of a cross inertial term in the momentum equation due to this geometry change. Results show that the unsteady modeling technique works over a wide variety of conditions. Reynolds numbers ranging from 15 to 75, and eccentricity ratios ranging from 0.25 to 0.82 were examined. Results of a benchmark model provided good agreement with experimental data (Jung, *et al.*, 1991b) for the prediction of the damping coefficient. The unsteady prediction of the damping coefficient varied less than 14% from experimental results, when experimental uncertainty is neglected. The unsteady damping coefficient results are within the error band when uncertainty is accounted for. The inertia coefficient is over-predicted by a factor of ~2 compared to the benchmark case.

A parametric study using the benchmark geometry for a variety of Reynolds numbers has been performed. This study shows that the damping coefficient prediction falls within the uncertainty band of Jung's experimental data, an improvement over Jung's own analytical predictions.

A second unsteady model parametric study was performed to observe the damper performance at various eccentricity ratios for a range of Reynolds numbers. The

variation of the eccentricity ratio has a large effect on the predictions of the damping (tangential) force component. As the eccentricity ratio increases, the damping force increases. However, the effect on the inertia (radial) force component is inconclusive. Further experimental investigation is necessary to determine the radial force variation with eccentricity ratio and confirm the predictions of the damping force.

Although the predicted radial and tangential forces may be comparable in magnitude, a typical rotor system will have many other sources of radial force (probably of greater magnitude than that of the damper); however, the system may not have any other source of tangential force approaching the magnitude provided by the damper.

In conclusion, it must be noted that the principle purpose of a squeeze film damper is to provide a damping (tangential) force to a rotordynamic system, not an inertial (radial) force. An unsteady analysis which can accurately predict the damping force over a variety of operating conditions is a valuable tool for rotordynamic analysis.

Acknowledgments

References

1. Jung, S.Y.; San Andres, L.A.; Vance, J.M.: "Measurements of Pressure Distributions and Force Coefficients in a Squeeze Film Damper Part I: Fully Open Ended Configuration," *Tribology Transactions*, Volume 34, No. 3, pp. 375-382, 1991.

2. Jung, S.Y.; San Andres, L.A.; Vance, J.M.: "Measurements of Pressure Distributions and Force Coefficients in a Squeeze Film Damper Part II: Partially Sealed Configuration," *Tribology Transactions*, Volume 34, No. 3, pp. 383-388, 1991.

3. San Andres, L.A: "Effect of Fluid Inertia on Force Coefficients for the Long Squeeze Film Damper," *Tribology Transactions*, Vol. 31, No. 3, pp. 370-375, 1988.

4. San Andres, L.A; Vance, J.M.: "Effect of Fluid Inertia on the Performance of Squeeze Film Damper Supported Rotors," *ASME Journal of Engineering for Gas Turbines and Power*, Vol. 110, pp. 51-57, January 1988.

5. San Andres, L.A; Vance, J.M.: "Effect of Fluid Inertia on Squeeze-Film Damper Forces for Small-Amplitude Circular-Centered Motions," *ASLE Transactions*, Vol. 30, No. 1, pp. 62-68, 1987.

6. San Andres, L.A; Vance, J.M.: "Effect of Fluid Inertia and Turbulence on the Force Coefficients for Squeeze-Film Dampers," *ASME Journal of Engineering for Gas Turbines and Power*, Vol. 108, pp. 332-339, April 1986.

7. Tichy, J.A.: "A Study of the Effect of Fluid Inertia and End Leakage in the Finite Squeeze Film Damper," *ASME Journal of Tribology*, Vol. 109, pp. 54-59, January 1987.

8. Tichy, J.A.: "Effects of Fluid Inertia and Viscoelasiticity on the One-Dimensional Squeeze-Film Bearing," *ASLE Transactions*, Vol. 27, No. 2, pp. 164-167, 1984.

9. Tichy, J.A.: "Effects of Fluid Inertia and Viscoelasiticity on Squeeze-Film Bearing Forces," *ASLE Transactions*, Vol. 25, No. 1, pp. 125-132, 1982.

10. Majumdar, A.K.: "A Generalized Fluid System Simulation Program to Model Flow Distribution in Fluid Networks," SvT Report No. 331-201-96-003, October 1996.

11. Vance, J.M.: Rotordynamics of Turbomachinery, pp. 240-247, J. Wiley & Sons, 1988.

12. Schallhorn, P.A.; Elrod, D.A.; Goggin, D.G.; Majumdar, A.K.: "A Fluid Circuit Model for Long Bearing Squeeze Film Damper Rotordynamics," *AIAA Journal of Propulsion and Power*, submitted for consideration of publication December, 1998.

13. Schallhorn, P.A.: Unsteady Analysis of the Fluid Film Forces in a Long Bearing Squeeze Film Damper, Ph.D. Dissertation, The University of Alabama in Huntsville, 1998.

14. Schallhorn, P.A.: "Unsteady Long Bearing Squeeze Film Damper Modeling for Circular Centered Orbits and Statically Eccentric Operation," SvT Report No. 611-022-98-002, November 1998.

15. Patankar, S., *Numerical Heat Transfer and Fluid Flow*, Hemisphere Publishing Co., New York, 1980.

16. Patankar, S., Karki, K., *Documentation of COMPACT-2D Version 3.1*, (User's Manual) Innovative Research, Inc., 1993.
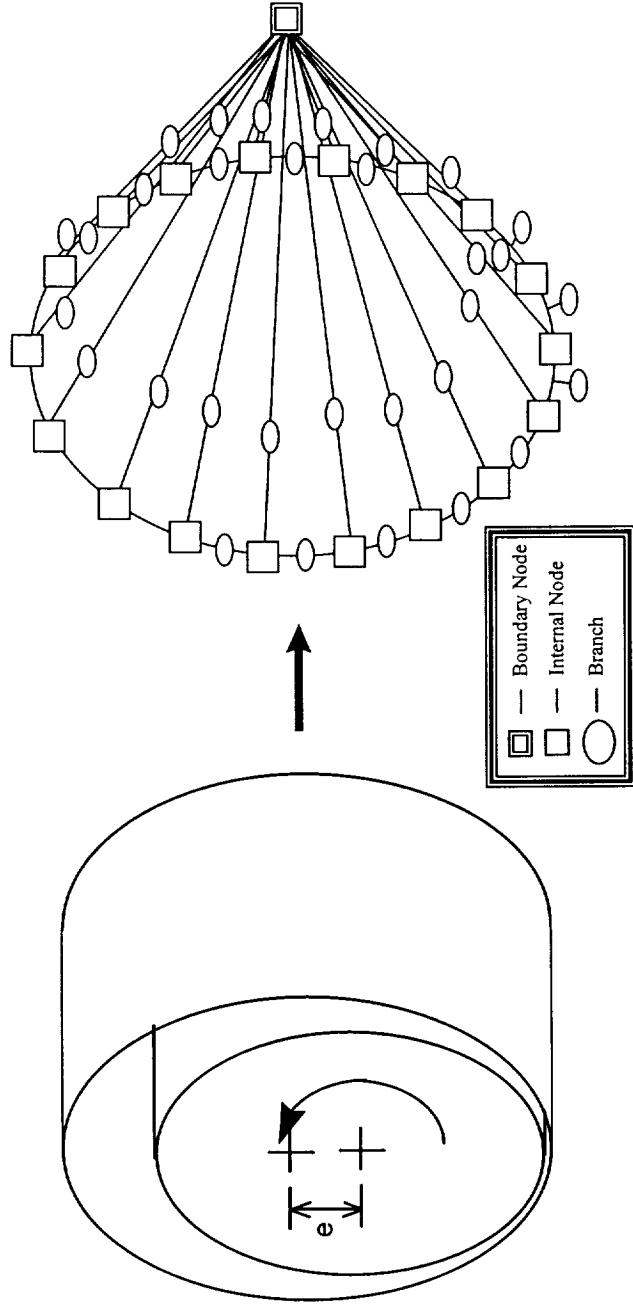
Figure 1: Unsteady Squeeze Film Damper Modeling

Table 1: Dimensionless Benchmark Rotordynamic Coefficient Comparison

	C_{tt}	D_{rr}
Unsteady Model Prediction	100.3	61.1
Jung, *et al.* Experimental Result	$\sim 89 \pm 11.37$	$\sim 29.5 \pm 12.58$
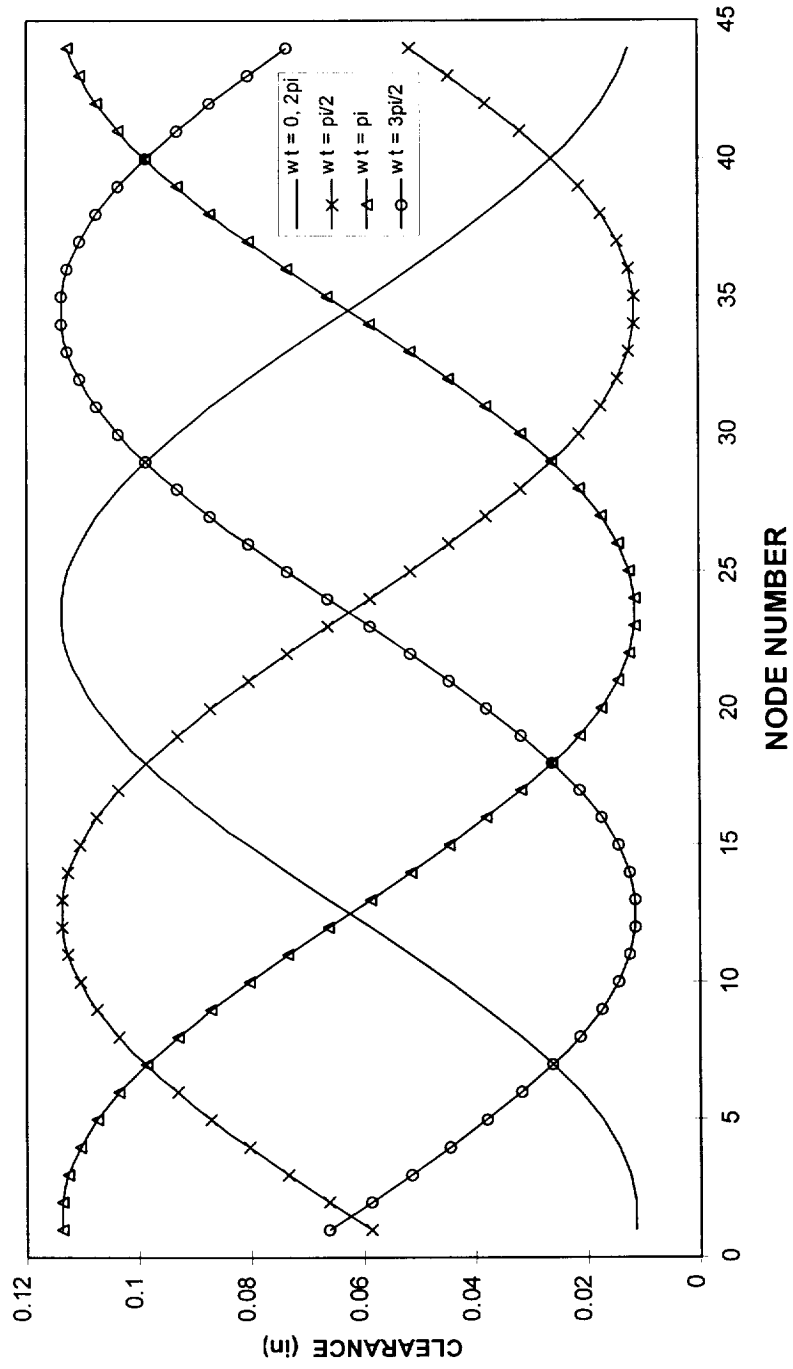
Figure 2: Unsteady Squeeze Film Damper Modeling Geometry Variation for Circular

Centered Orbits (CCO)

19
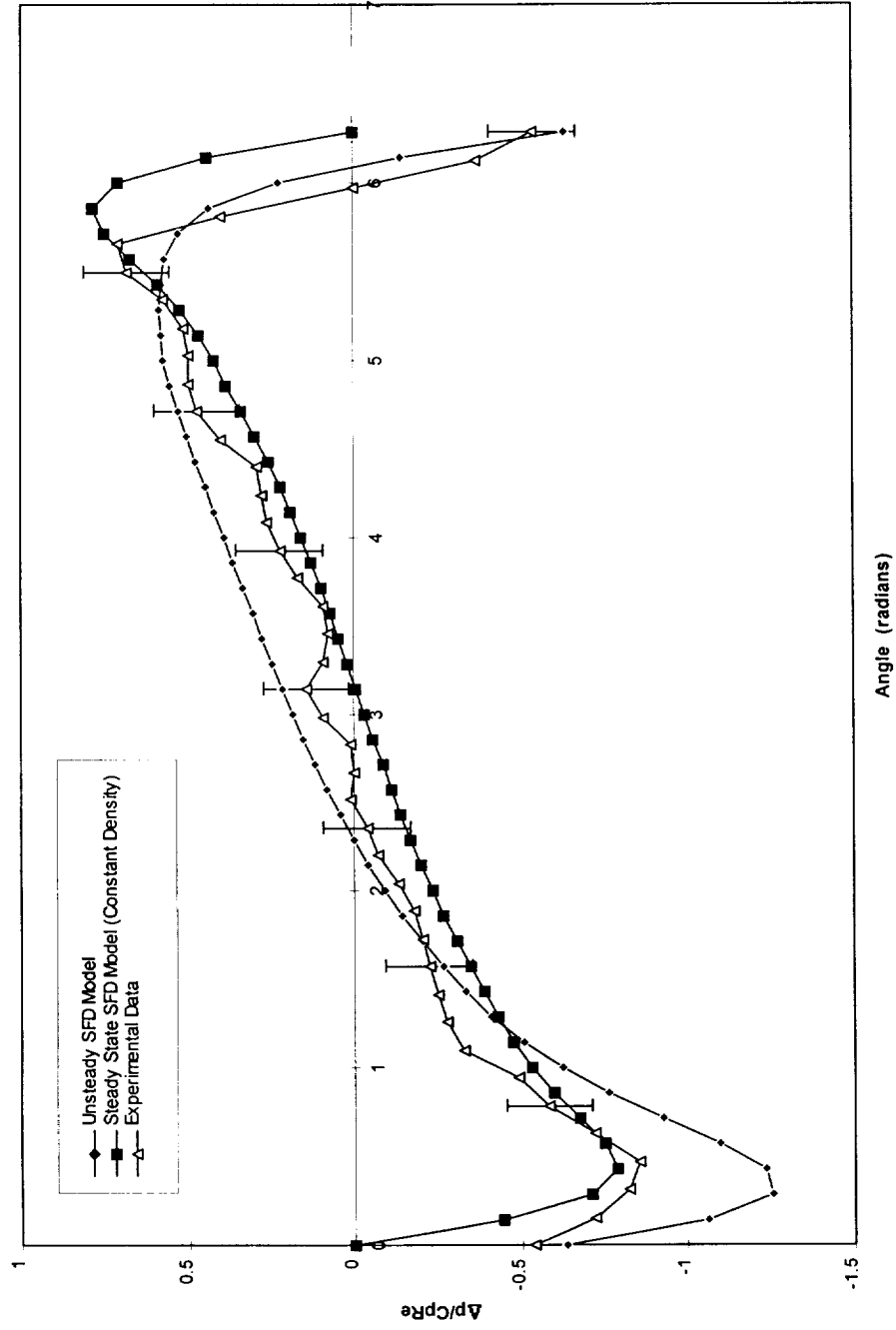
Figure 3: Benchmark Unsteady Model Dimensionless SFD Pressure Profile Predictions

with Steady State Model and Jung's Data Overlay

20
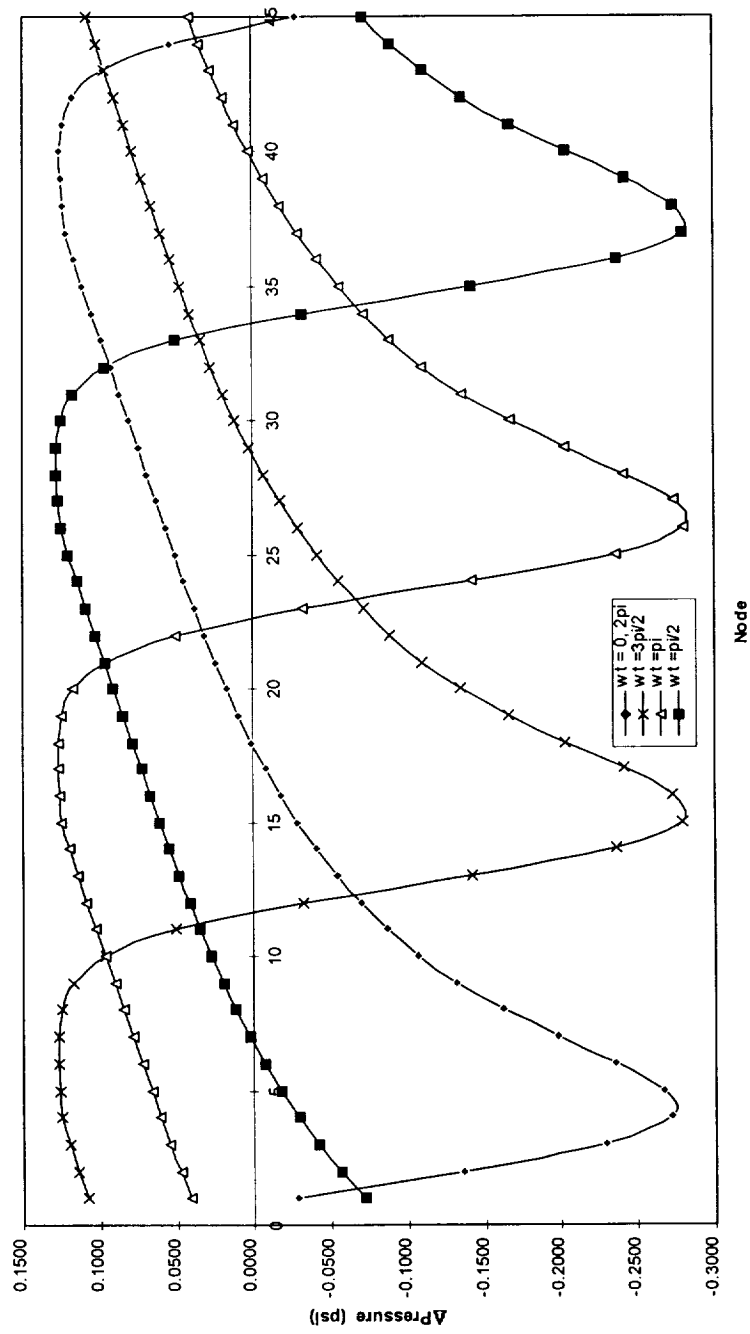
Figure 4: GFSSP Predicted Pressure Profile vs. Node Over One Period for Benchmark
Case
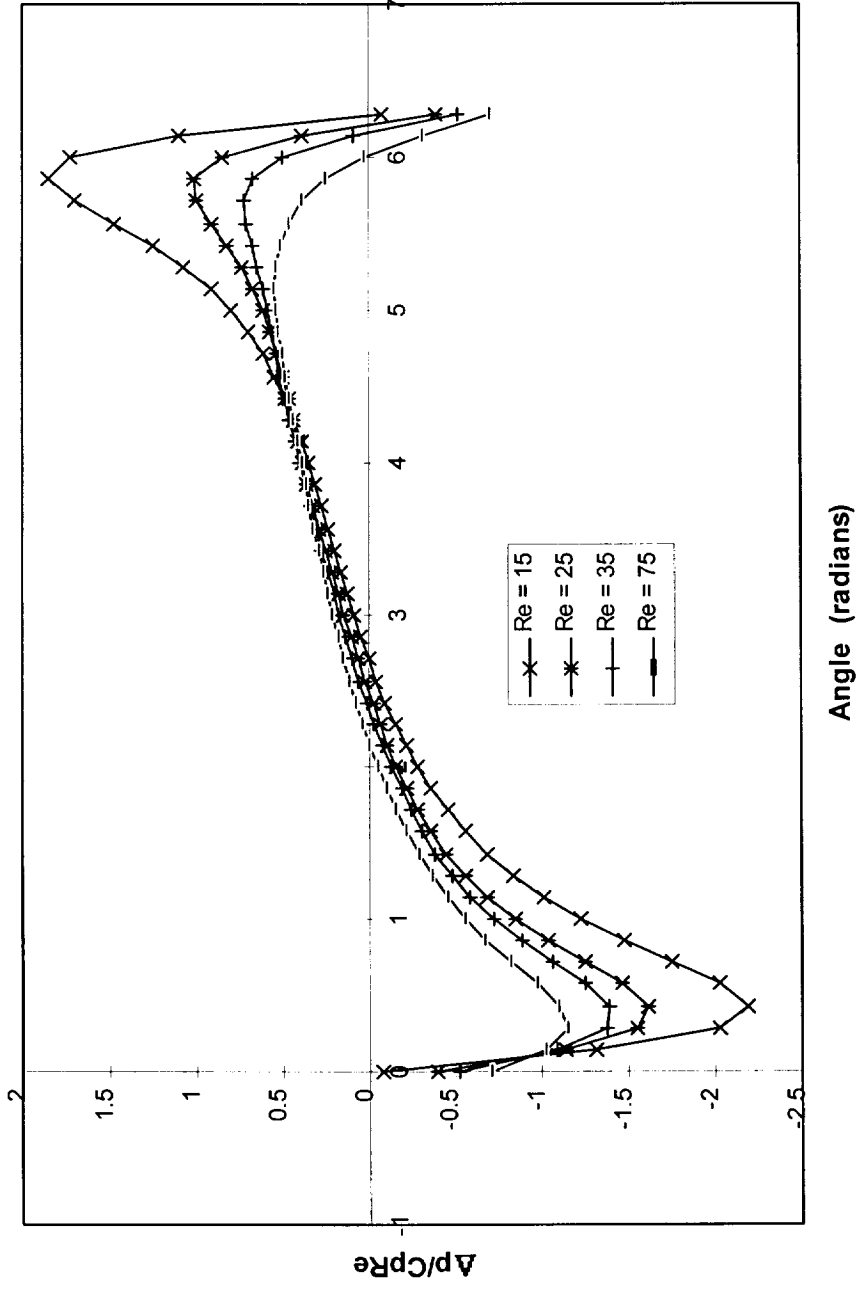
Figure 5: Dimensionless SFD Pressure Distribution *vs.* Angle at Various Reynolds
Numbers
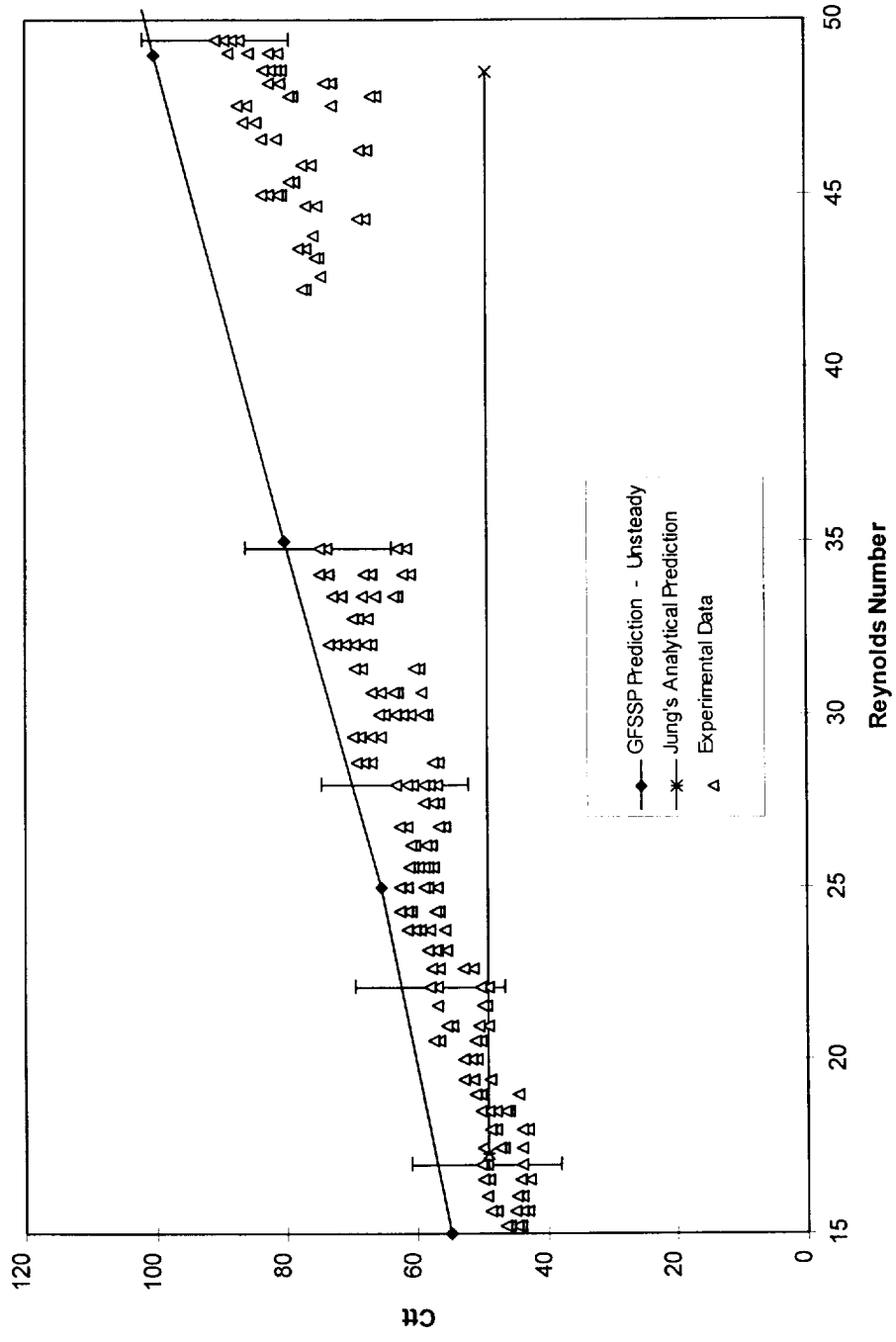
Figure 6: Unsteady GFSSP Model Dimensionless Damping Coefficient Predictions

23
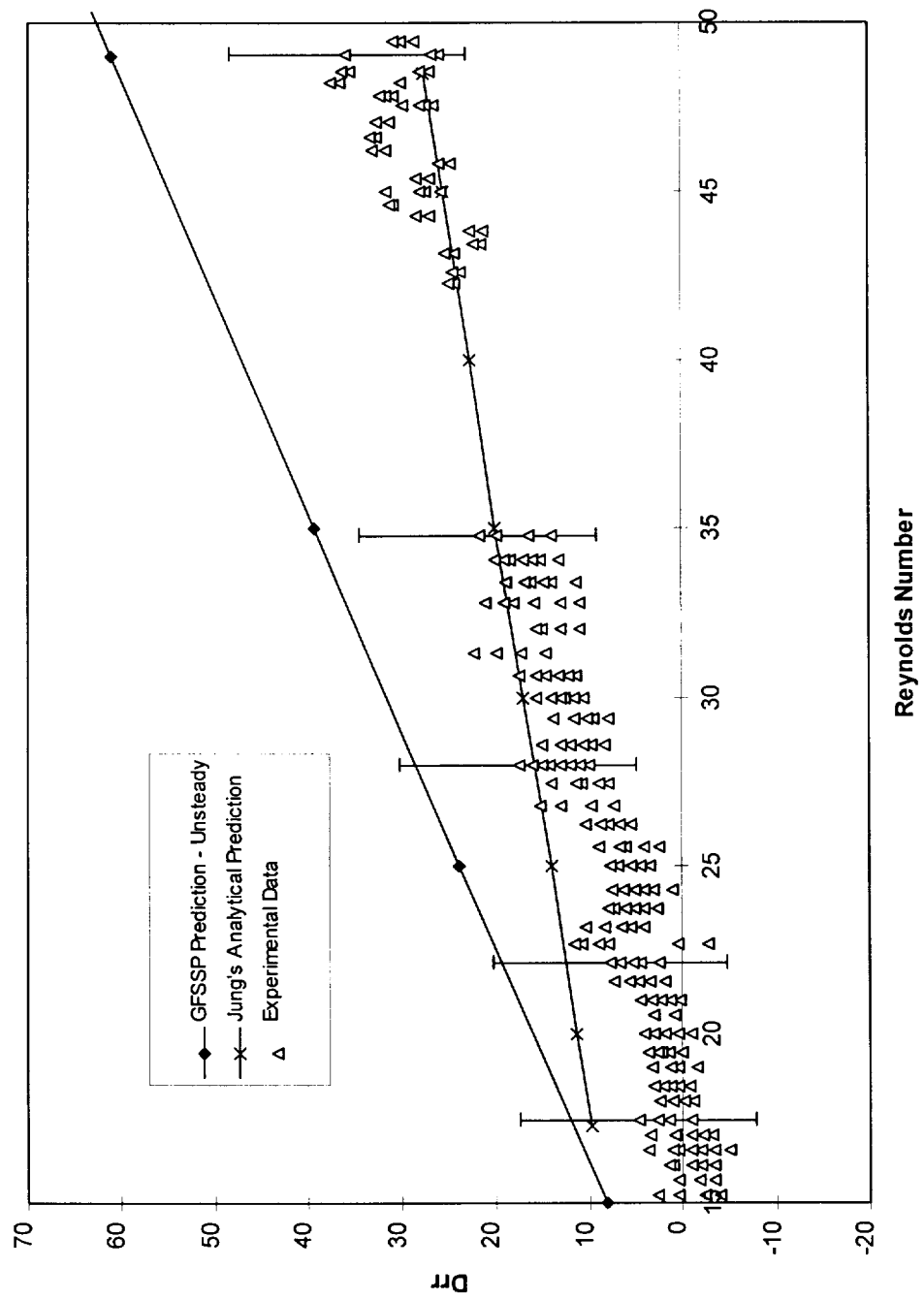
Figure 7: Unsteady GFSSP Model Dimensionless Inertia Coefficient Predictions

24
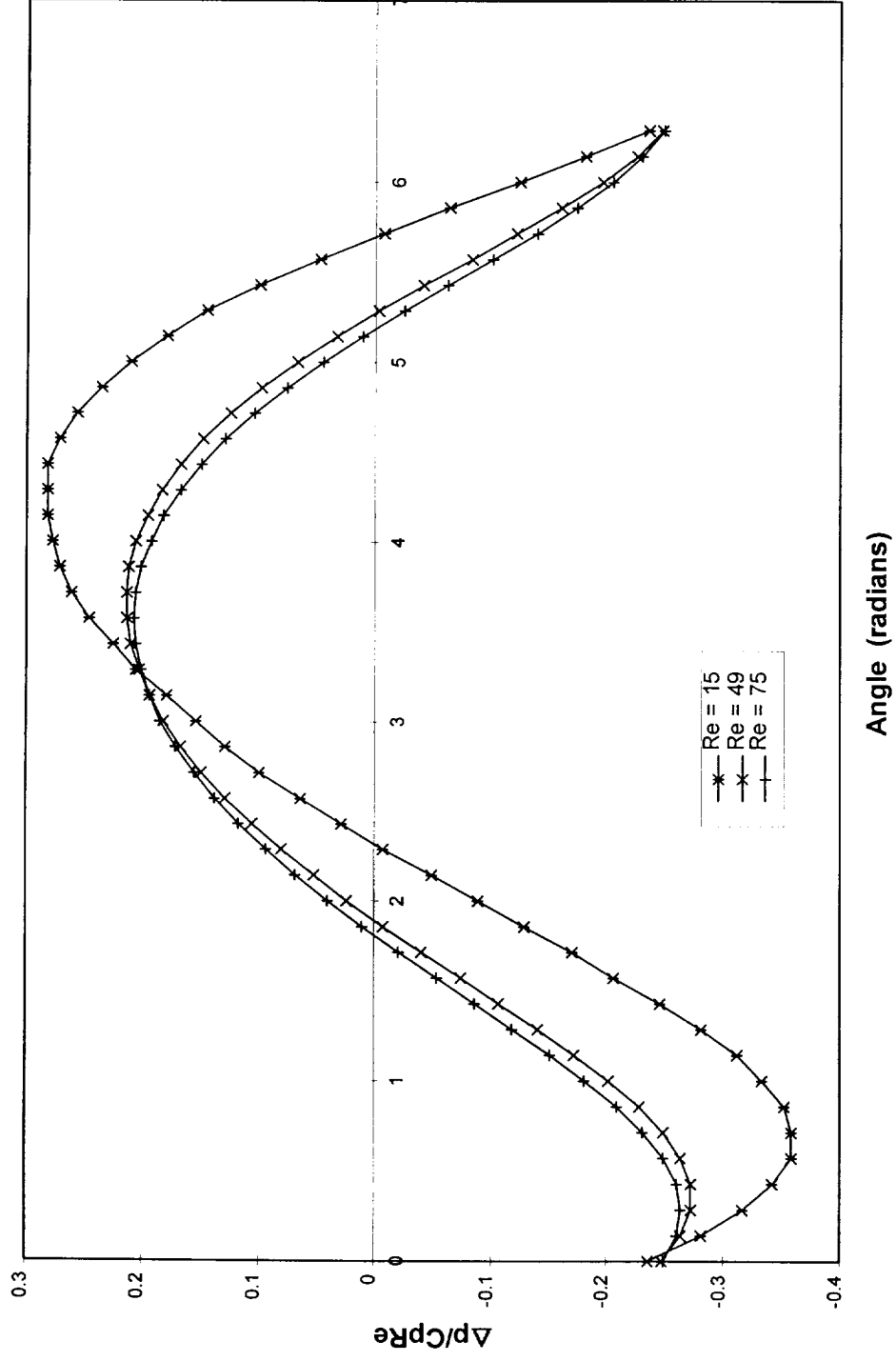
Figure 8: Dimensionless SFD Pressure Distribution *vs.* Angle for ε = 0.25
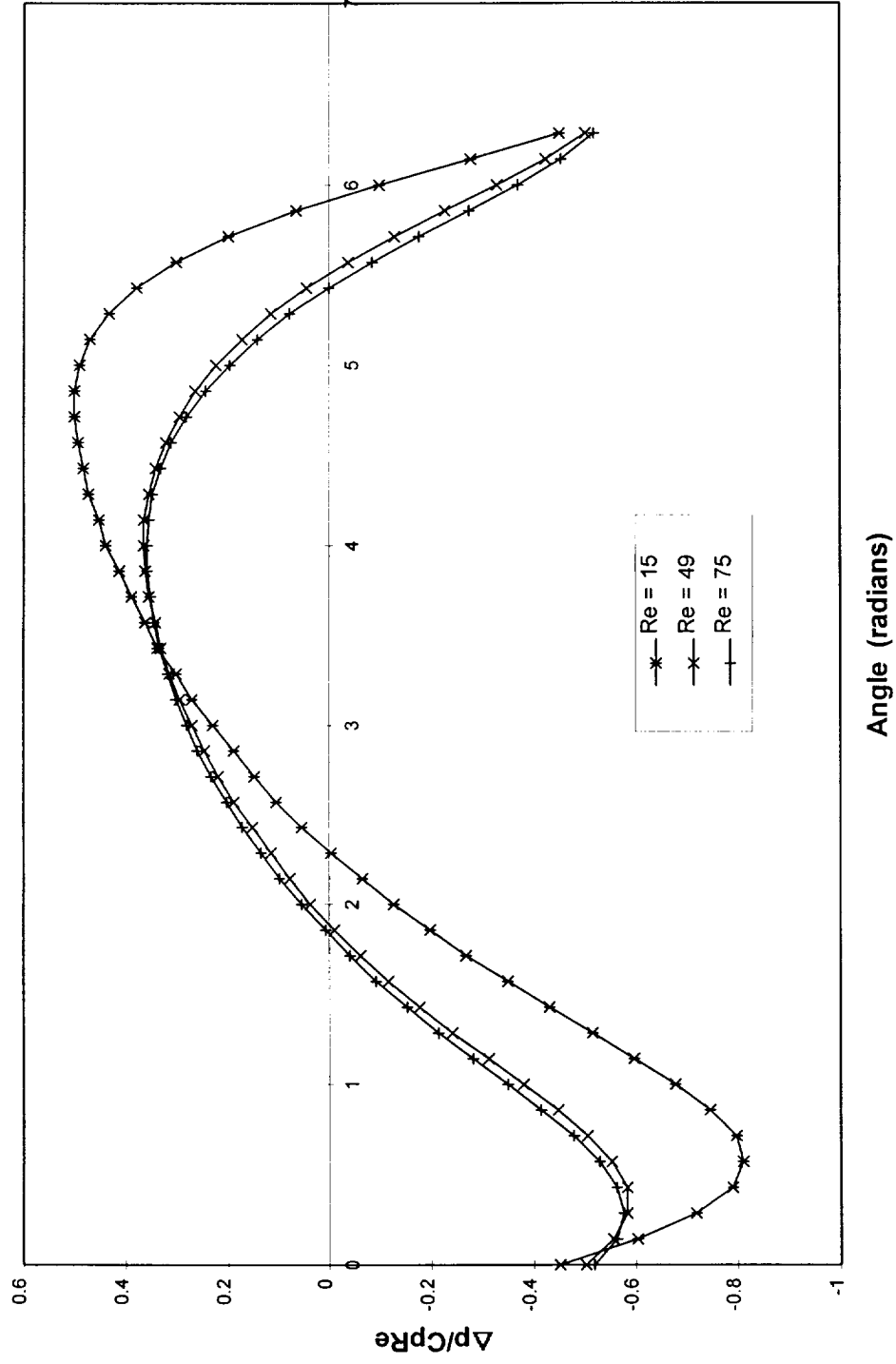
Figure 9: Dimensionless SFD Pressure Distribution vs. Angle for ε = 0.50
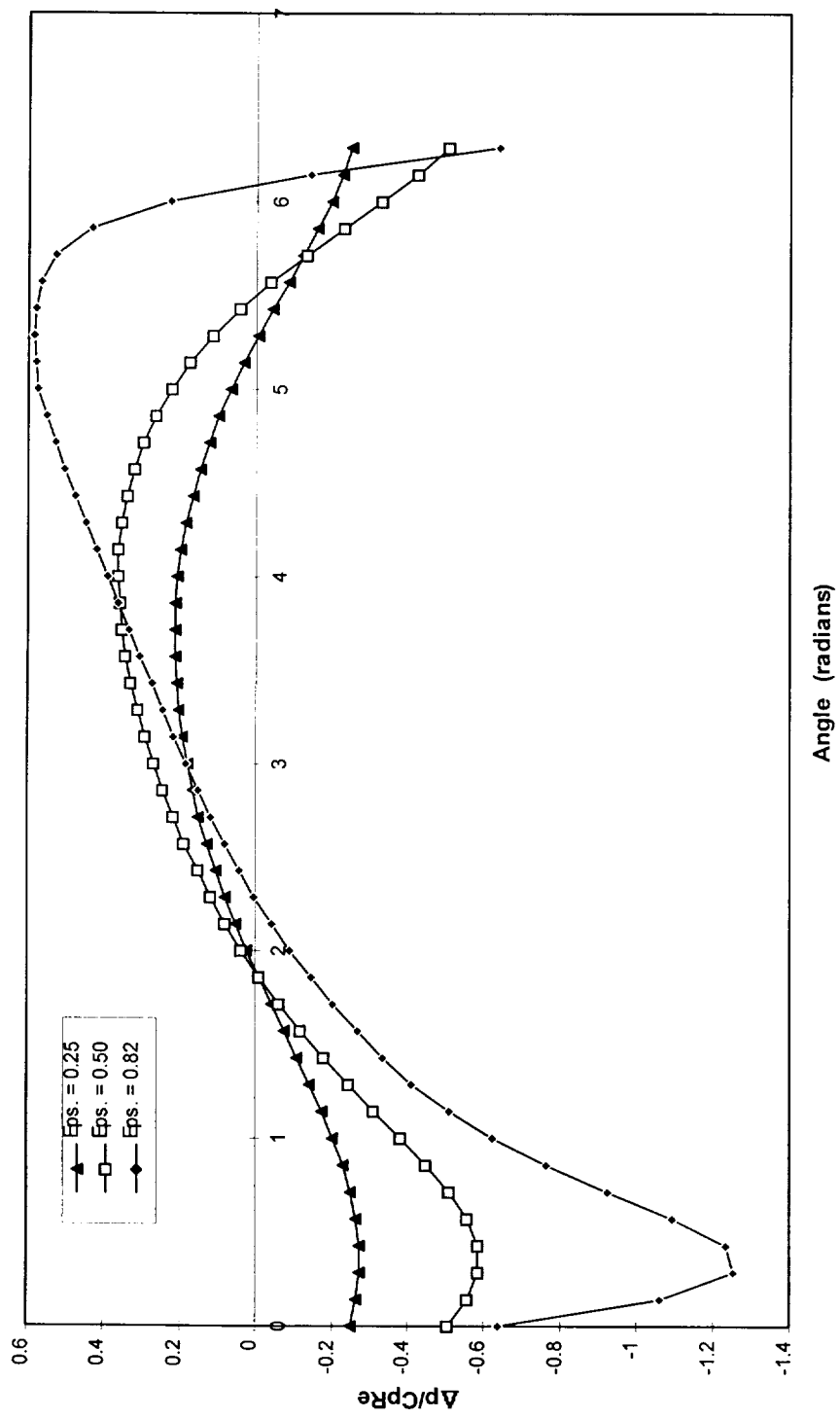
Figure 10: Dimensionless SFD Pressure Distribution Comparison vs. Angle for Re = 49
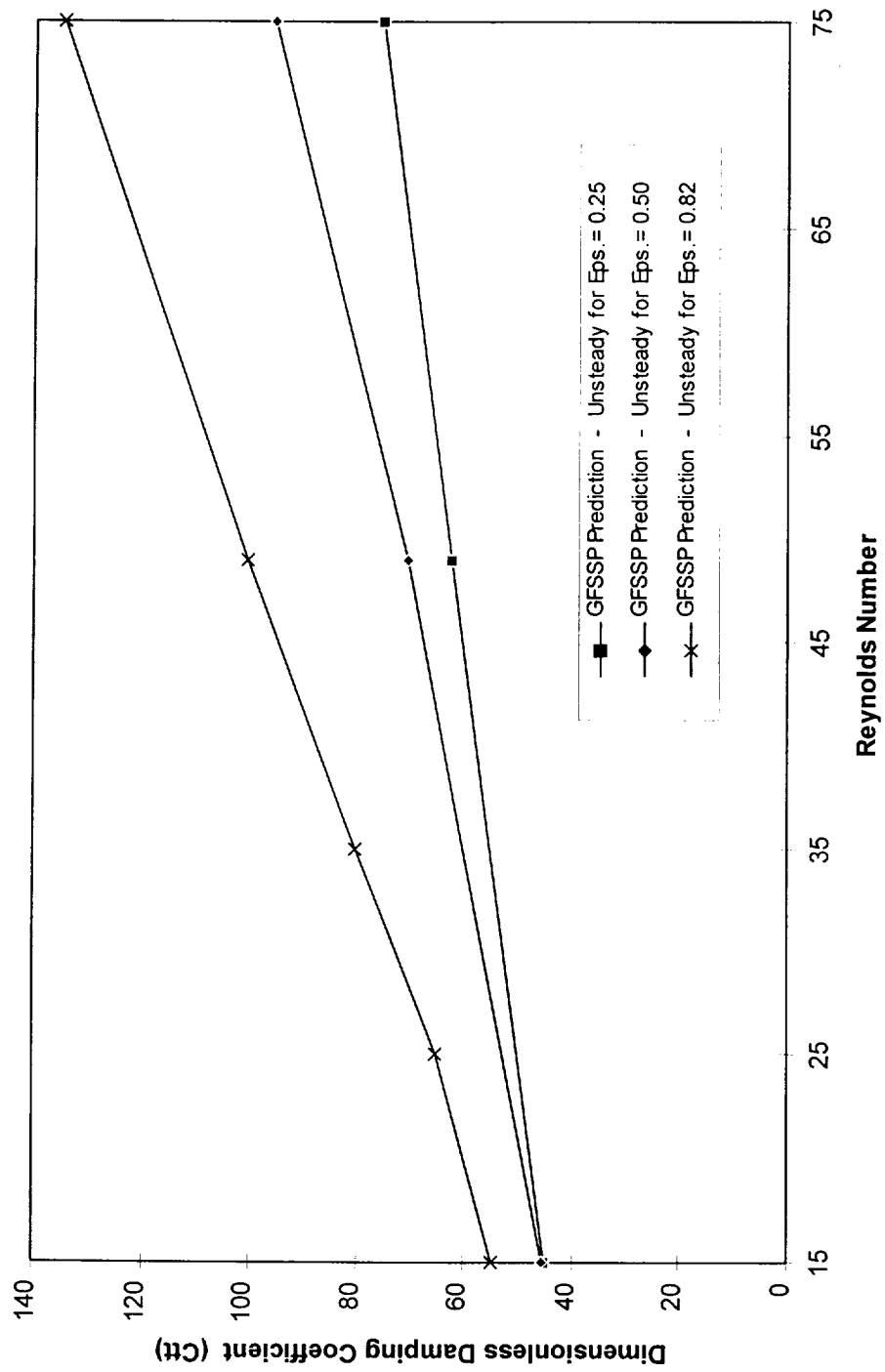
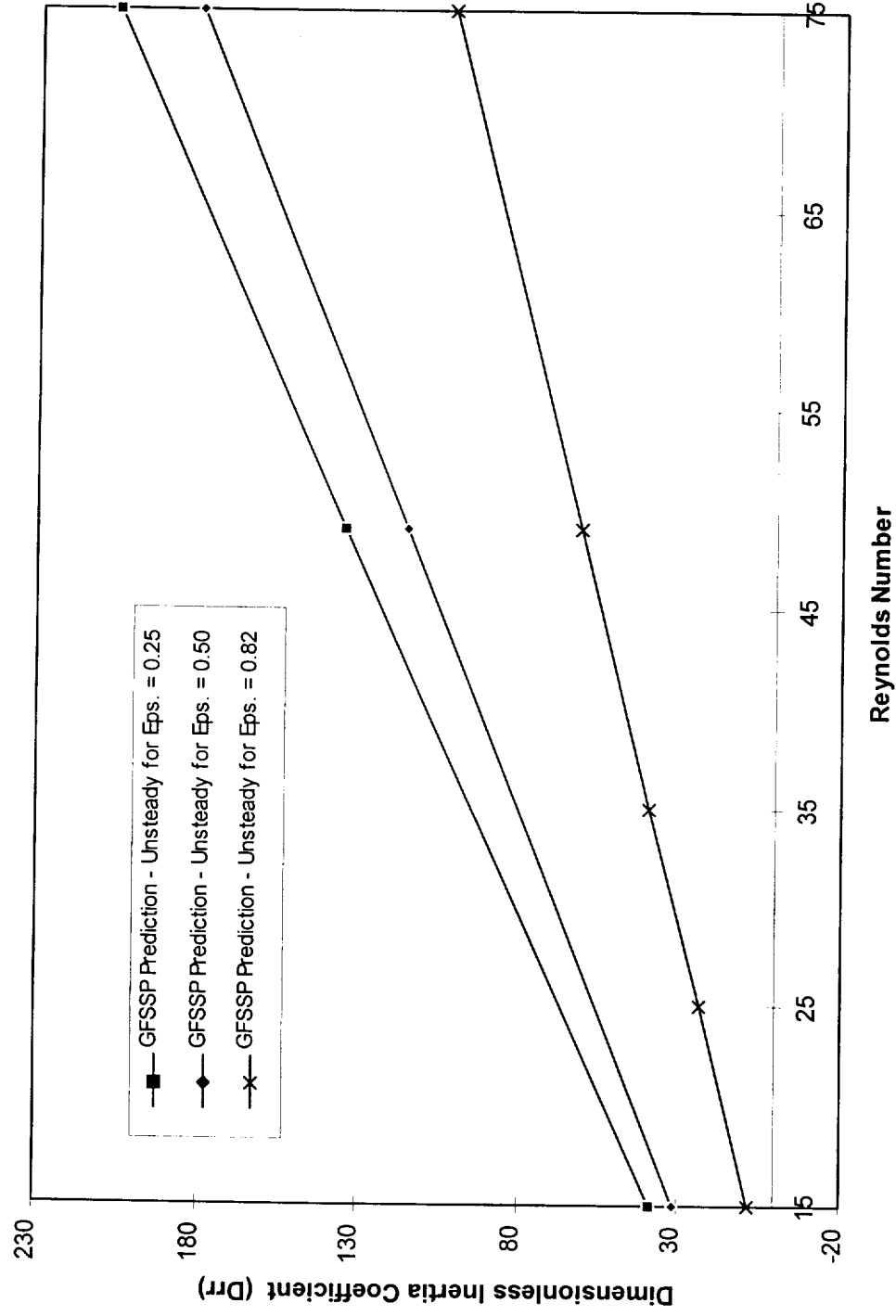Figure 11: Unsteady GFSSP Model Dimensionless Damping Coefficient - Parametric Study Results

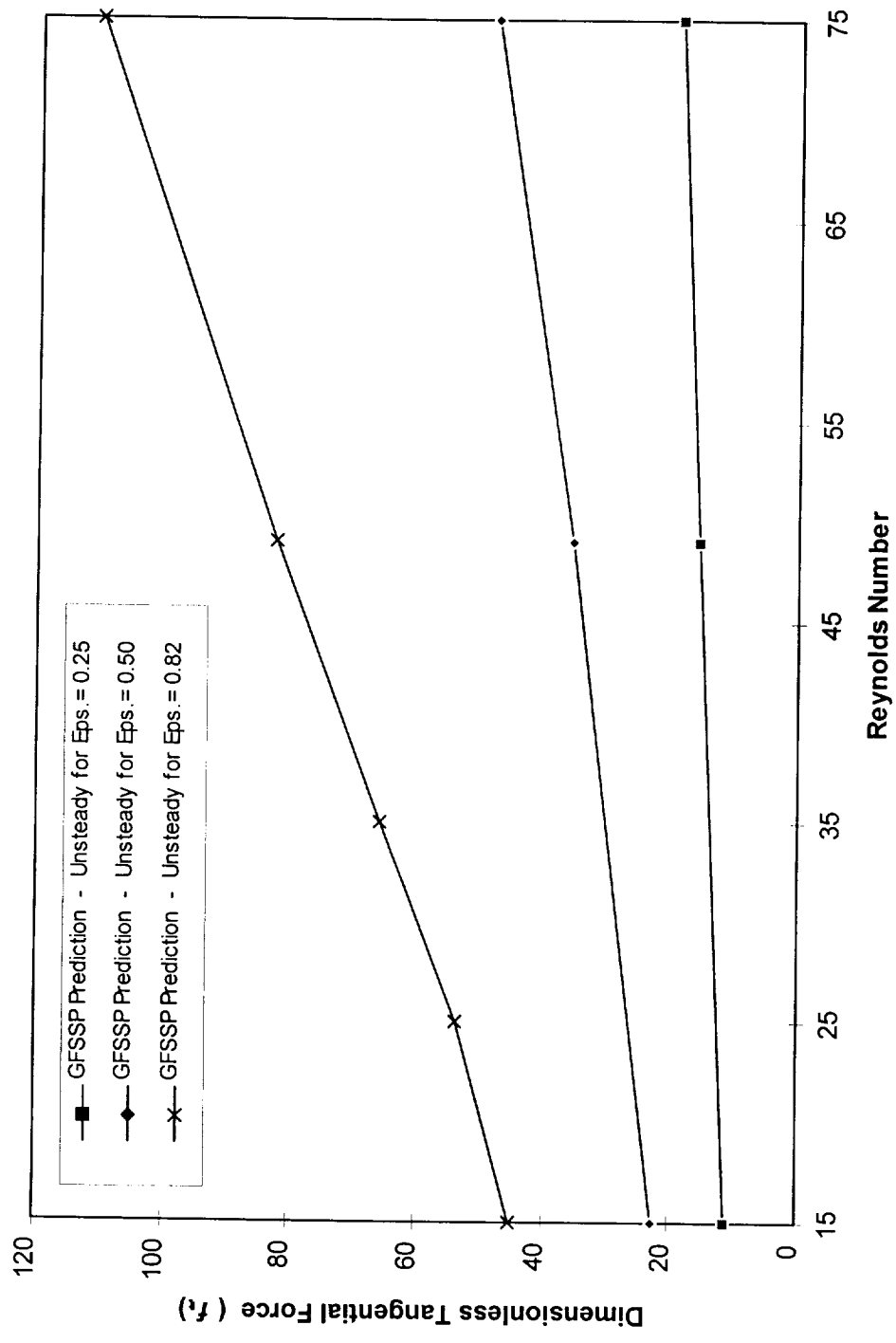Figure 12: Unsteady SFD Model Dimensionless Inertia Coefficient - Parametric Study Results

29

Figure 13:Unsteady SFD Model Dimensionless Tangential Force - Parametric Study
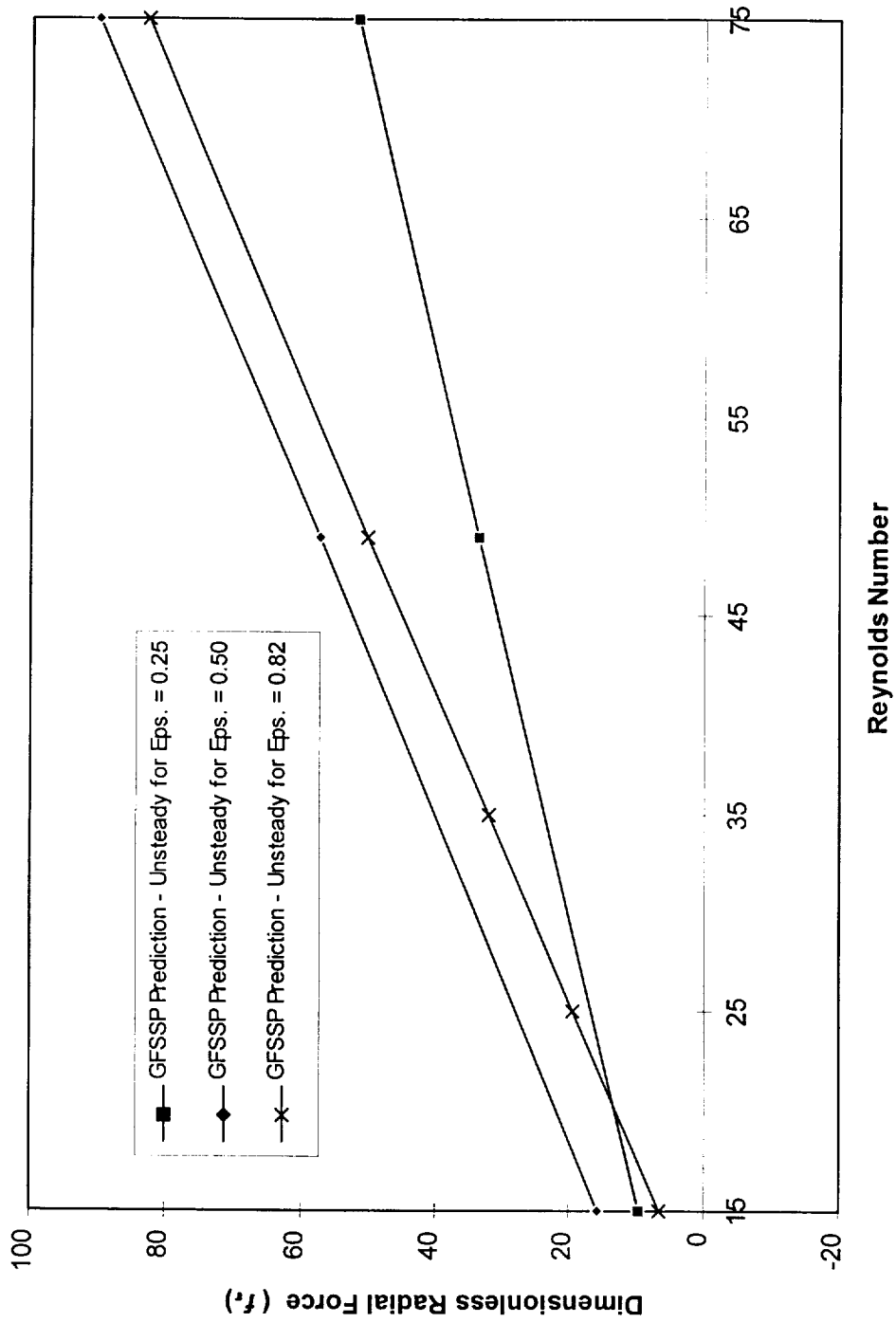Results

Figure 14: Unsteady SFD Model Dimensionless Radial Force - Parametric Study Results